Solar Wind Charge Exchange Soft X-Ray Emissions in the Magnetosphere during an Interplanetary Coronal Mass Ejection Compared to Its Driven Sheath

Yingjie Zhang, Tianran Sun, Chi Wang, Li Ji, Jennifer. A. Carter, Xiaowei Zhao, Steve Sembay, Dimitra Koutroumpa, Ying D. Liu, Guiyun Liang, et al.

The Astrophysical Journal Letters, 932:L1 (8pp), 2022 June 10 https://doi.org/10.3847/2041-8213/ac7521

Solar Wind Charge Exchange Soft X-Ray Emissions in the Magnetosphere during an Interplanetary Coronal Mass Ejection Compared to Its Driven Sheath

Yingjie Zhang[1], Tianran Sun[1], Chi Wang[1,2], Li Ji[3], Jennifer. A. Carter[4], Steve Sembay[4], Dimitra Koutroumpa[5], Ying D. Liu[1,2], Guiyun Liang[6], Wenhao Liu[3], Wei Sun[3], and Xiaowei Zhao[1]
[1] State Key Laboratory of Space Weather, National Space Science Center, Chinese Academy of Sciences, Beijing 100190, People's Republic of China
trsun@swl.ac.cn
[2] College of Earth and Planetary Sciences, The University of Chinese Academy of Sciences, Beijing, People's Republic of China; cw@swl.ac.cn
[3] Purple Mountain Observatory, Chinese Academy of Sciences, Nanjing, Jiangsu 210008, People's Republic of China
[4] School of Physics and Astronomy, The University of Leicester, Leicester, UK
[5] LATMOS/IPSL, CNRS, UVSQ Université Paris-Saclay, Sorbonne Université, Guyancourt, France
[6] Key Laboratory of Optical Astronomy, National Astronomical Observatories, Chinese Academy of Sciences, Beijing 100101, People's Republic of China
Received 2022 April 20; revised 2022 May 30; accepted 2022 May 31; published 2022 June 9

Abstract

Soft X-ray emissions from solar wind charge exchange (SWCX) are applied in a recently developed approach to study the magnetosphere using panoramic soft X-ray imaging. This study represents the first attempt to distinguish magnetospheric SWCX emissions observed by XMM-Newton during the impact of an interplanetary coronal mass ejection (ICME) and its driven sheath on Earth. In addition, data from the Advanced Composition Explorer (ACE) were available during this same observational period, which is rare in previous studies. Results showed that SWCX emissions peaked during the ICME at approximately 2.3 times the mean of the observation period, although the solar wind flux decreased to a much lower level. A comparison of spectral results with ion data probed by ACE revealed that high ionization states in the ICME effectively enhanced line emission intensity for heavy ions (e.g., Ne, Mg, and Al). Thus, despite a low proton flux, elevated high-valence ion abundance in the ICME favors magnetospheric soft X-ray observations. Furthermore, the fitted X-ray flux of ion line emissions was consistent with elemental abundance ratios determined in situ by ACE, particularly for C^{5+}, C^{6+}, Ne^{9+}, Mg^{11+}, and Mg^{12+}. This confirms the viability of spectral diagnosis of SWCX emissions as a new method for remotely analyzing high-state ion distributions in solar wind. A time-correlated or two-stage efficiency factor is further suggested to better estimate X-ray intensity during an ICME impact, which was ~1.7 times higher in the ICME than in the sheath.

Unified Astronomy Thesaurus concepts: Solar coronal mass ejections (310); Solar-terrestrial interactions (1473); Diffuse x-ray background (384); Solar wind (1534); X-ray astronomy (1810)

1. Introduction

Solar wind charge exchange (SWCX) occurs when a high-valence solar wind ion interacts with a neutral atom to acquire an electron and transition to excited states, followed by the release of one or more soft X-ray or UV photons during electron relaxation (Cravens 1997). These events have been widely observed on Earth (Snowden et al. 2004, 2009; Carter & Sembay 2008; Ezoe et al. 2010; Carter et al. 2011, 2012; Ishikawa et al. 2013), Mars (Dennerl et al. 2006), Jupiter (Branduardi-Raymont et al. 2007), a comet (Lisse et al. 1996), and the Moon (Collier et al. 2014). The soft X-ray intensity along a specific line of sight can be estimated as (Cravens 2000; Sun et al. 2015, 2019, 2021)

$$I = \frac{1}{4\pi}\int \alpha n_{\rm H} n_{\rm sw} v_{\rm rel} dr (\rm keV\ cm^{-2}\ s^{-1}\ sr^{-1}), \quad (1)$$

where $n_{\rm H}$ and $n_{\rm sw}$ are the densities of neutral hydrogen and solar wind protons, respectively. The relative velocity $v_{\rm rel}$ can be calculated from the solar wind velocity $v_{\rm sw}$ and the thermal velocity $v_{\rm th}$ as follows: $v_{\rm rel} = \sqrt{v_{\rm sw}^2 + v_{\rm th}^2}$. The SWCX efficiency factor (alpha) can then be determined using

$$\alpha = \sum_{Xqj} \alpha_{Xqj} = \sum_{Xqj} \sigma_{Xqj} \left[\frac{X^{q+}}{\rm O}\right]\left[\frac{\rm O}{n_{\rm sw}}\right] (\rm eV\ cm^2), \quad (2)$$

where α_{Xqj} is the charge exchange efficiency factor for the energy level j after a solar wind ion X (in the charge state q) interacts with neutral hydrogen, σ_{Xqj} is the charge exchange cross section, $\left[\frac{X^{q+}}{\rm O}\right]$ is the elemental abundance ratio (defined as the ratio of a specific ion to oxygen ions), and $\left[\frac{\rm O}{n_{\rm sw}}\right]$ is the ratio of oxygen ions to solar wind proton density.

Coronal mass ejections (CMEs) are explosive events on the Sun that release large amounts of plasma and magnetic flux into the solar system. The interplanetary remnant of a CME is an interplanetary coronal mass ejection (ICME), the propagation of which generates a shockwave at the leading edge and compresses ambient solar wind, forming an ICME-driven sheath. The solar wind properties in the ICME (ejected from the Sun) and ICME-driven sheath (ambient solar wind) are apparently different, as illustrated in Figure 1. First, the solar wind proton flux in the ICME-driven sheath increases due to compression and decreases in the ICME due to expansion. Second, the ions in most ICMEs have higher ionization states compared to the ICME-driven sheath (Richardson & Cane 2010; Richardson 2014). In addition, the interplanetary magnetic field (IMF) in an ICME typically exhibits a long-term

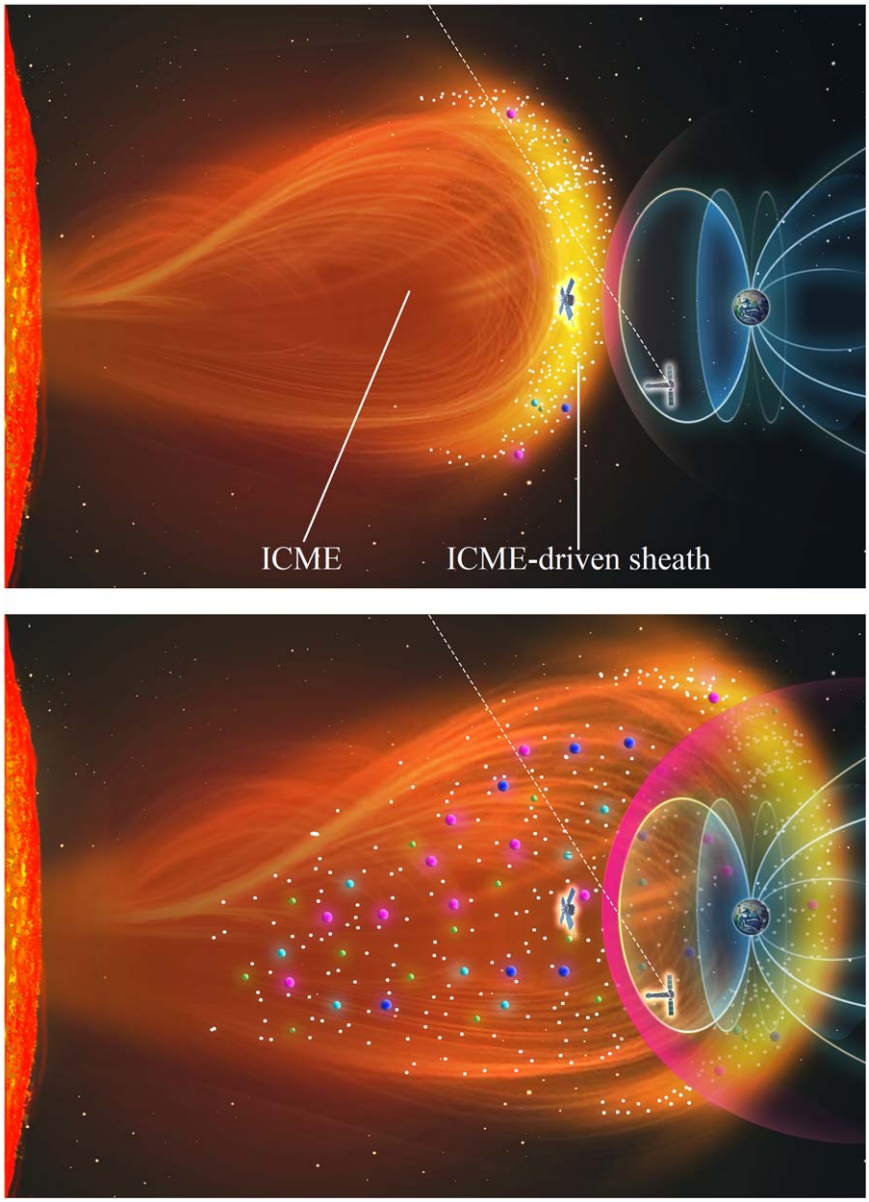

Figure 1. A schematic diagram (not to scale) of magnetospheric SWCX soft X-ray emissions during the successive impact of an ICME-driven sheath (top) and ICME (bottom) on Earth. Magnetospheric SWCX emissions (bright magenta) were observed remotely by XMM-Newton, for which the line of sight is represented by dotted lines. Solar wind protons (small white spheres) and high-state ions (colored spheres) were observed in situ by ACE.

southward component that is more geoeffective, potentially causing geomagnetic storms or substorms. Previous studies have analyzed ICME and ICME-driven sheaths as a single unit and attributed the enhanced SWCX intensity primarily to an increase in solar wind flux (Carter et al. 2010; Ezoe et al. 2011; Ishi et al. 2019; Asakura et al. 2021). However, SWCX emission features can differ significantly in an ICME and ICME-driven sheath. For example, solar wind flux is higher in the sheath and the elemental abundance ratio is similar to that of the ambient solar wind, resulting in higher SWCX intensity (see Equation (1)). Regardless, while the elemental abundance ratio may be higher in the ICME, the solar wind flux can be much lower, leading to unclear estimates of SWCX emission levels.

While SWCX soft X-ray emissions are a source of contamination in astrophysical observations, they are also important signals containing information about geospace environments. On Earth, the soft X-ray emissions produced by SWCX are concentrated in the magnetosheath and cusp regions, which can be used for large-scale remote magnetospheric imaging (Branduardi-Raymont et al. 2012; Collier et al. 2012; Sibeck et al. 2018). On this basis, the Solar wind Magnetosphere Ionosphere Link Explorer (SMILE; Branduardi-Raymont et al. 2018; Wang & Branduardi-Raymont 2020), a joint ESA–CAS soft X-ray imager with a uniquely large field of view ($16^\circ \times 27^\circ$), is currently under implementation and planned for launch in 2024 $\sim$ 2025. One of the most important scientific goals of the SMILE mission is to study interactions between the solar wind and magnetosphere during ICME, since successive ICMEs could produce superstorms that would cause enormous damage to human society (Liu et al. 2014, 2019). Furthermore, it is also important for evaluating the SWCX background in astronomical observations, since many studies solely use solar wind proton flux as a

measure of soft X-ray emission intensity (Henley & Shelton 2010, 2012).

Assessing SWCX emission levels caused by solar ejecta is critical for X-ray imaging during ICME-induced space weather events, since the ICME itself is more geoeffective than its driven sheath. Moreover, due to a lack of in situ measured solar wind ion data, neither the telemetry spectral results nor the true SWCX efficiency factor (alpha) can be verified or calculated when evaluating soft X-ray intensities in previous studies. As such, this study represents the first attempt to distinguish magnetospheric SWCX emissions during the impact of an ICME and its driven sheath on Earth. In addition, this study is a rare joint observation of Advanced Composition Explorer (ACE) and XMM-Newton during an ICME event.

As demonstrated in Figure 1, this study includes multiple steps. (1) We analyze the difference in magnetospheric SWCX emissions observed by XMM-Newton during the successive impacts of an ICME-driven sheath and ICME. (2) We compare the spectral results obtained remotely by XMM-Newton with the ion data determined in situ by ACE. (3) We calculate the time-varying alpha value using ion data collected by ACE. Section 2 describes data analysis. Section 3 shows the result. Sections 4 and 5 provide discussions and conclusions.

2. Data Analysis

The XMM-Newton original data files (ODFs) were acquired from the XMM-Newton science archive.[7] Science Analysis System (SAS) software (version 18.0.0)[8] and HEASoft (version 6.28)[9] were used for data processing and analysis. Current calibration files (CCFs) were released on 2021 April 27. The ICME of interest was not observed as part of the routine XMM-Newton observational schedule because Earth's magnetosphere was not the target of the astronomical study. Specifically, the target was 3C 35 (01:12:02.19, +49:28:35.0, J2000) for this observation with Obs.ID 0655610101. The data used for analysis were extracted from the region shown in Figure 5. This included the target magnetospheric SWCX emission and seven complex backgrounds: astronomical point sources, soft proton flares (SPs), particle background, cosmic background, instrumental lines, residual soft proton contamination, and heliospheric SWCX emissions.

Following the method described in Carter et al. (2010) and the cookbook for analyzing extended objects,[10] we first adopted the astrophysical point-source lists (113 sources in total) available from the XMM-Newton science archive to create a region filter that removed events within a radius of 35″ centered on each source. Second, we used the espfilt task, which fitted a Gaussian to the histogram of lightcurve values and created good time intervals (GTIs) with a count rate in the range of 2.5σ around the roughly Gaussian peak. We only selected GTIs with long continuous exposure times, since SPs can be highly variable, slowly varying, or a complex combination as shown in Figures 2(e)–(g). Third, we applied the evqpb task to produce a particle background spectrum from the filter wheel closed (FWC) set. This spectrum was then compared with the observed spectrum in the 7.5–9.2 keV energy band to derive scaling factors for MOS1 (1.015), MOS2 (1.101), and pn (1.149). Fourth, a three-component model was included in the spectral fit to represent the cosmic background. This involved an unabsorbed plasma component representing emissions from the local hot bubble or heliosphere, an absorbed plasma component representing emissions from the hotter halo, and an absorbed power-law component representing the unresolved extragalactic X-ray background. The APEC model was used for plasma components and the phabs model was used for absorption. A spectrum of the soft X-ray background acquired from the ROSAT all-sky survey (RASS) was included to constrain parameters and jointly fit the MOS and pn spectra in the 0.275–6.5 keV energy band, using an average galactic H I column density of 1.18×10^{21} cm^{-2}.[11] Fifth, instrumental lines for Al K_α and Si K_α were excised by adding a zero-width Gaussian model with an energy of $E \sim 1.49$ keV for MOS and pn and an energy of $E \sim 1.75$ keV for MOS only. Sixth, the power-law components representing the residual SP were separate models and were assigned separate diagonal response matrices for MOS and pn. Finally, since SWCX emissions from the target magnetosphere and the background heliosphere had similar characteristics, both were jointly fitted by a set of zero-width Gaussian models with energies fixed at the likely emission lines for solar wind ions. The charge exchange cross sections (Bodewits et al. 2007) calculated at 600 km s^{-1} (closest to the observed speed) were applied to C, N, and O. A series of empirical emission transitions for heavy elements were also added at higher energies.

3. Observations on 2011 February 18

Figure 2 shows the solar wind data measured by WIND and ACE[12] from 2011 February 17 to 20, including XMM-Newton observations made during this period. Our estimate of the leading ICME edge is near 8:30 UT (orange vertical dashed line), after the interplanetary shock seen at 1:20 UT on February 18 (black arrow). The evidence for this ICME edge is as follows: (1) $T_p < 0.5T_{\rm exp}$ in panel (a), as indicated by the green shadows. Here, $T_{\rm exp}$ is the expected temperature determined from the empirical correlation $V_{\rm sw} - T_p$ (Richardson & Cane 2004). (2) The proton density drops suddenly from approximately 19.4 to 8.9 cm^{-3} in panel (b). (3) $O^{7+}/O^{6+} > 1$ in panel (c). (4) $\langle Q \rangle_{\rm Fe} > 12$ in panel (d) (Zurbuchen & Richardson 2006). This study focuses on protons and ions, more details for this event can be found in Liu et al. (2020). XMM-Newton first observed a high-density ICME-driven sheath and then a low-density ICME during GTIs from 5:15 to 10:45 UT (blue vertical lines). In this process, the line of sight for XMM-Newton shifted from near the subsolar region to the magnetosheath flank as XMM-Newton moved toward Earth. This effect can be observed in panels (h) and (i).

The top of Figure 3 shows the time-varying X-ray flux for SWCX emissions based on the fitting of 11 spectra extracted at intervals of 1800 s (the absent pn interval is due to soft proton flares). In the ICME-driven sheath, the X-ray flux for SWCX emissions decreased with solar wind proton flux. However, although the solar wind flux decreased to a much lower level in the ICME, the X-ray flux peaked near 10:00 UT, which was 2.3 (MOS1), 2.3 (MOS2), and 3.0 (pn) times the mean of the entire observation period. Similar distribution is also revealed by the red crosses in Figures 2(e), (f), and (g). The bottom of Figure 3

[7] http://nxsa.esac.esa.int/nxsa-web/
[8] https://www.cosmos.esa.int/web/xmm-newton/sas-threads/
[9] https://heasarc.gsfc.nasa.gov/lheasoft/
[10] https://heasarc.gsfc.nasa.gov/docs/xmm/esas/cookbook/xmm-esas.html
[11] https://heasarc.gsfc.nasa.gov/cgi-bin/Tools/xraybg/xraybg.pl
[12] https://cdaweb.gsfc.nasa.gov/index.html/

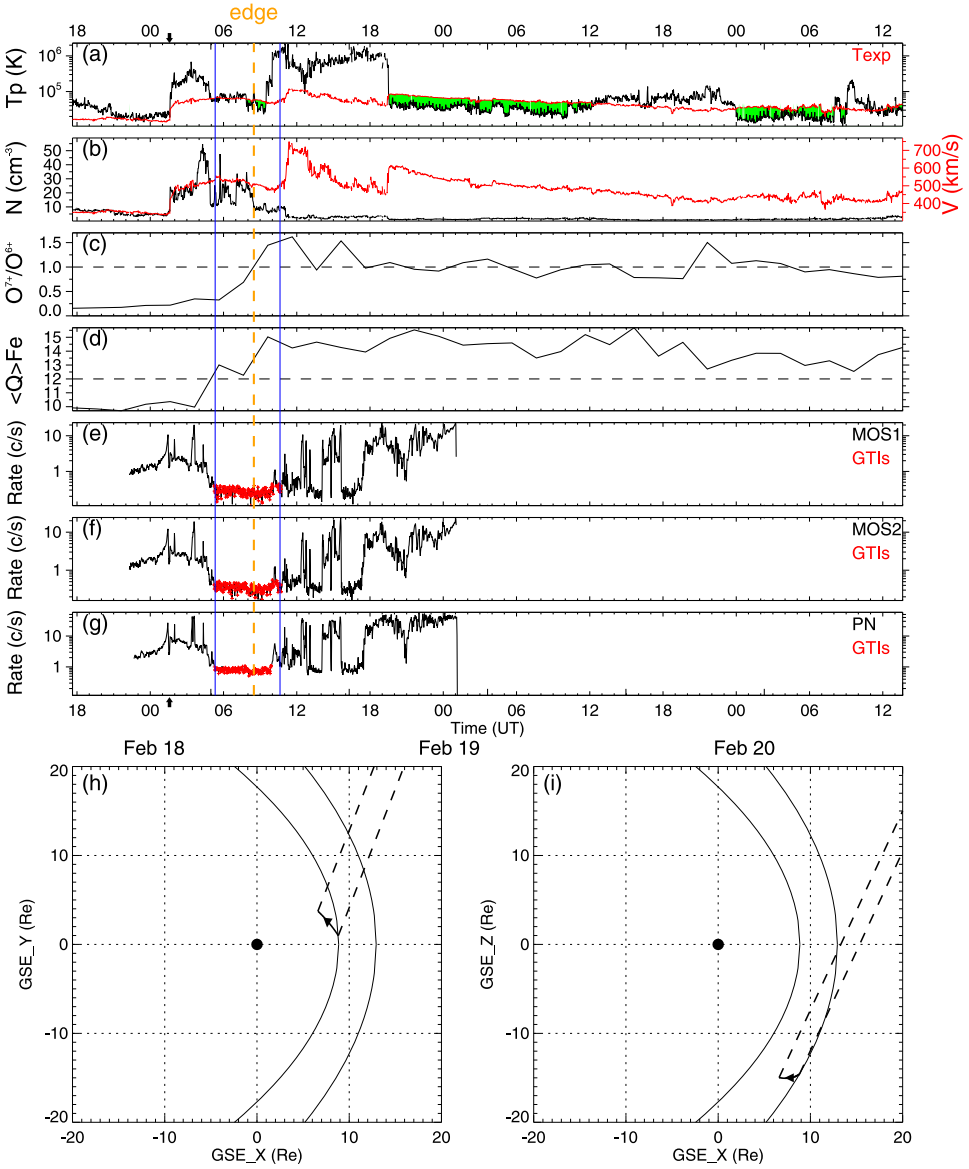

Figure 2. Solar wind data: (a) proton temperature and expected temperature (red), (b) proton density and velocity (red), (c) ratio of O^{7+} to O^{6+}, and (d) average iron charge states. XMM-Newton data: (e), (f), (g) 2.5–8.5 keV light curves and GTIs (red), (h), (i) orbital positions during GTIs (solid lines with arrow), line of sight (dashed lines), and calculated average positions for magnetopause and bow shock (Shue et al. 1997; Khan & Cowley 1999) (gray lines). Black arrows: interplanetary shock. Vertical lines: GTI boundaries (blue) and estimated ICME leading edge (orange dashed).

shows the best-fitting SWCX spectra extracted from the interval centered at 7:00 UT in the ICME-driven sheath and at 10:00 UT in the ICME. It was evident that line emissions in both intervals were rich and the intensity of O^{8+} was higher than that of O^{7+}, which had previously been observed as a typical feature of magnetospheric SWCX emissions disturbed by an ICME (Carter et al. 2010; Ishi et al. 2019; Asakura et al. 2021). Furthermore, not only were there ion emission lines in the ICME from C, N, and O with similar total intensity as in the ICME-driven sheath, but also those of Ne, Mg, and Al, with significantly enhanced intensities. This effect caused SWCX emissions to reach a maximum in the ICME.

Figure 4 shows the fitted X-ray flux for each ion line emission, observed 2 hr elemental abundance ratios, and calculated alpha values. As seen in the right panel, the X-ray flux for C^{6+}, Ne^{9+}, Mg^{11+}, Mg^{12+}, and Al^{13+} increased significantly, while that of C^{5+}, N^{6+}, and N^{7+} decreased distinctly. In contrast, O, Fe, Ne^{10+}, and Si did not show significant variations. As seen in the left panel, ion data for N, Al, and higher charged Ne and Si were absent because they were not in the detection range for ACE. The ratio of oxygen ions to proton density decreased, while most elemental abundance ratios increased, excluding C^{5+} and Fe. The degree of enhancement in these cases was also significantly higher than the reductions. The value of alpha, as shown in the middle panel, was calculated using dynamic cross sections with only the measured abundance ratios for C^{5+}, C^{6+}, O^{7+}, O^{8+}, Ne^{9+}, and Mg^{11+}, due to a lack of cross sections available for other ions. With the exception of C^{5+} and O^{7+}, alpha values generally increased. It is suggested that a sudden increase of velocity after 10:30 (Figure 2(b)) tends to be a reason for the inconsistency between calculated alpha and the 2 hr averaged (9:30–11:30 UT) abundance ratio for O^{7+}, which decreased the size of the cross section. This sudden velocity change was caused by the successive impacts of two CMEs. Additional details concerning how the two CMEs produced complex

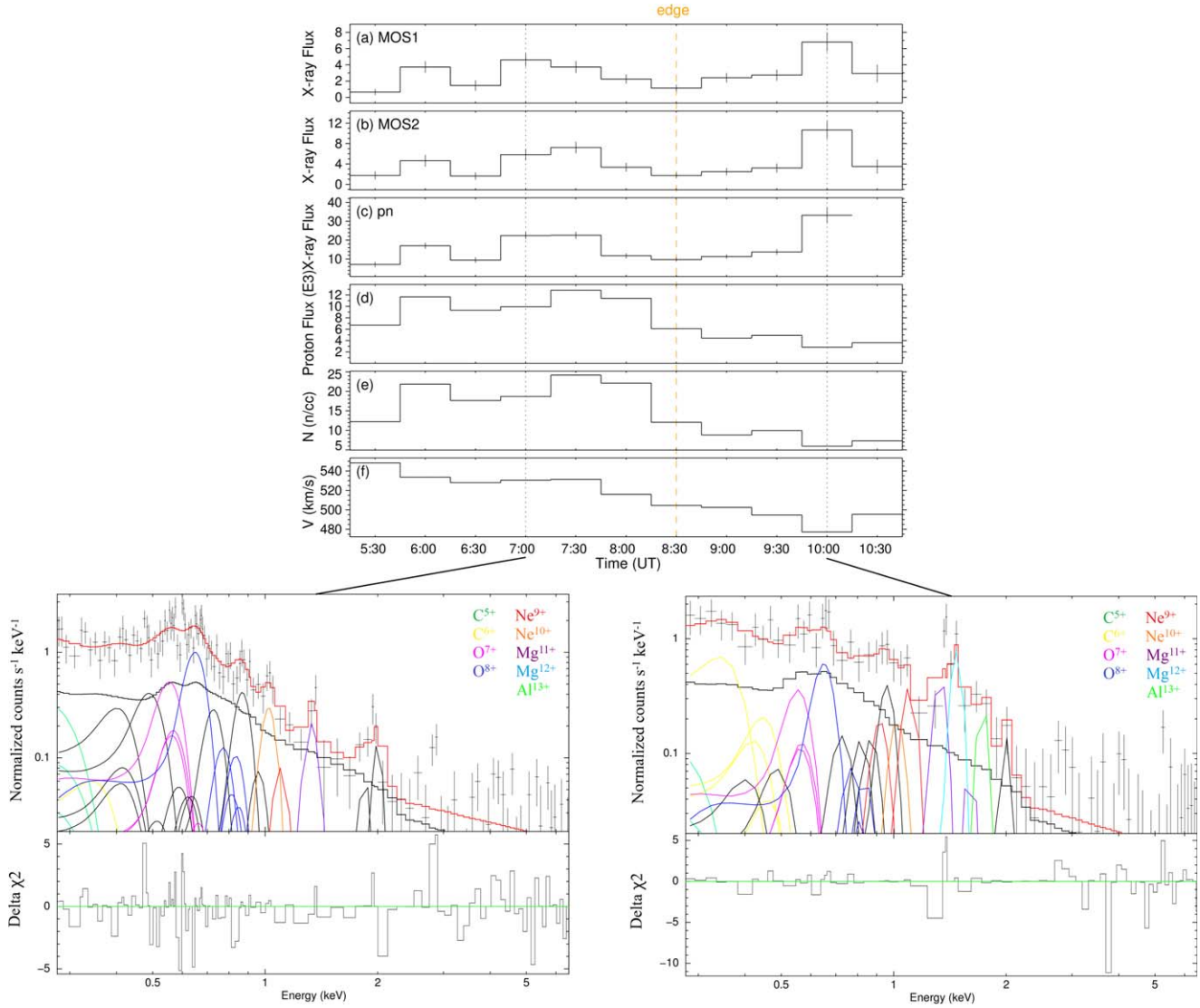

Figure 3. Top: (a), (b), (c) fitted X-ray flux for SWCX emissions measured in units of 10^{-8} erg cm^{-2} s^{-1} sr^{-1}. Half-hourly average solar wind proton data: (d) flux, (e) density, and (f) velocity. Vertical orange dashed line: estimated ICME leading edge. Bottom: SWCX spectral model fitted to the background-subtracted pn spectrum (similar for MOS, not shown here), extracted from the interval centered at 7:00 UT (left) and 10:00 UT (right). The ion emission lines are represented by Gaussian lines, where N, Fe, and Si are in black. The cosmic background is represented by the black curve, and the sum of all models is represented by the red curve. The best-fit reduced chi square is 1.054 (left) and 1.226 (right).

ejecta can be found in Liu et al. (2020). A comparison of the spectral results and solar wind ion data showed that an elevated abundance of highly charged ions in the ICME can substantially increase the level of SWCX emissions. In addition, the fitted X-ray flux of ion line emissions was consistent with solar wind elemental abundance ratios, particularly for C^{5+}, C^{6+}, Ne^{9+}, Mg^{11+}, and Mg^{12+}. The X-ray flux for SWCX emissions reached a maximum in the interval from 9:45 to 10:15 UT, while ion abundance ratios reached a maximum near 9:30 UT. These values are reasonable considering the 2 hr resolution of ion data.

4. Discussion

4.1. Characteristics of SWCX Emissions in the ICME-driven Sheath and ICME

The heliospheric SWCX emission was simulated using solar activity in 2011, the history of alpha values, and solar wind proton flux time-series developed from propagation times (Koutroumpa et al. 2006, 2007, 2009; Koutroumpa 2012; Kaaret et al. 2020). The heliospheric SWCX emission throughout the observation period (5:30–11:30 UT) displayed a monotonic decrease beginning at $6.9 \pm 0.96 \times 10^{-9}$ erg cm^{-2} s^{-1} sr^{-1} and ending at $4.3 \pm 0.64 \times 10^{-9}$ erg cm^{-2} s^{-1} sr^{-1}. Since SWCX models include emissions from both the magnetosphere and heliosphere, any increase in SWCX emissions is directly attributable to the magnetosphere. Rather than considering the ICME and its driven sheath as a whole, we studied the different characteristics of magnetospheric SWCX emissions during the successive impact of an ICME-driven sheath and ICME on Earth. The top panel of Figure 1 illustrates the increased magnetospheric SWCX emissions after the impact of an ICME-driven sheath, and the bottom panel shows even higher SWCX emissions increased with high-state ion abundance during subsequent ICME impact (i.e., Ne, Mg, and Al), although solar wind proton flux decreased significantly. This study demonstrates that even higher SWCX emissions with increased high-state ion abundance in the ICME favors magnetospheric soft

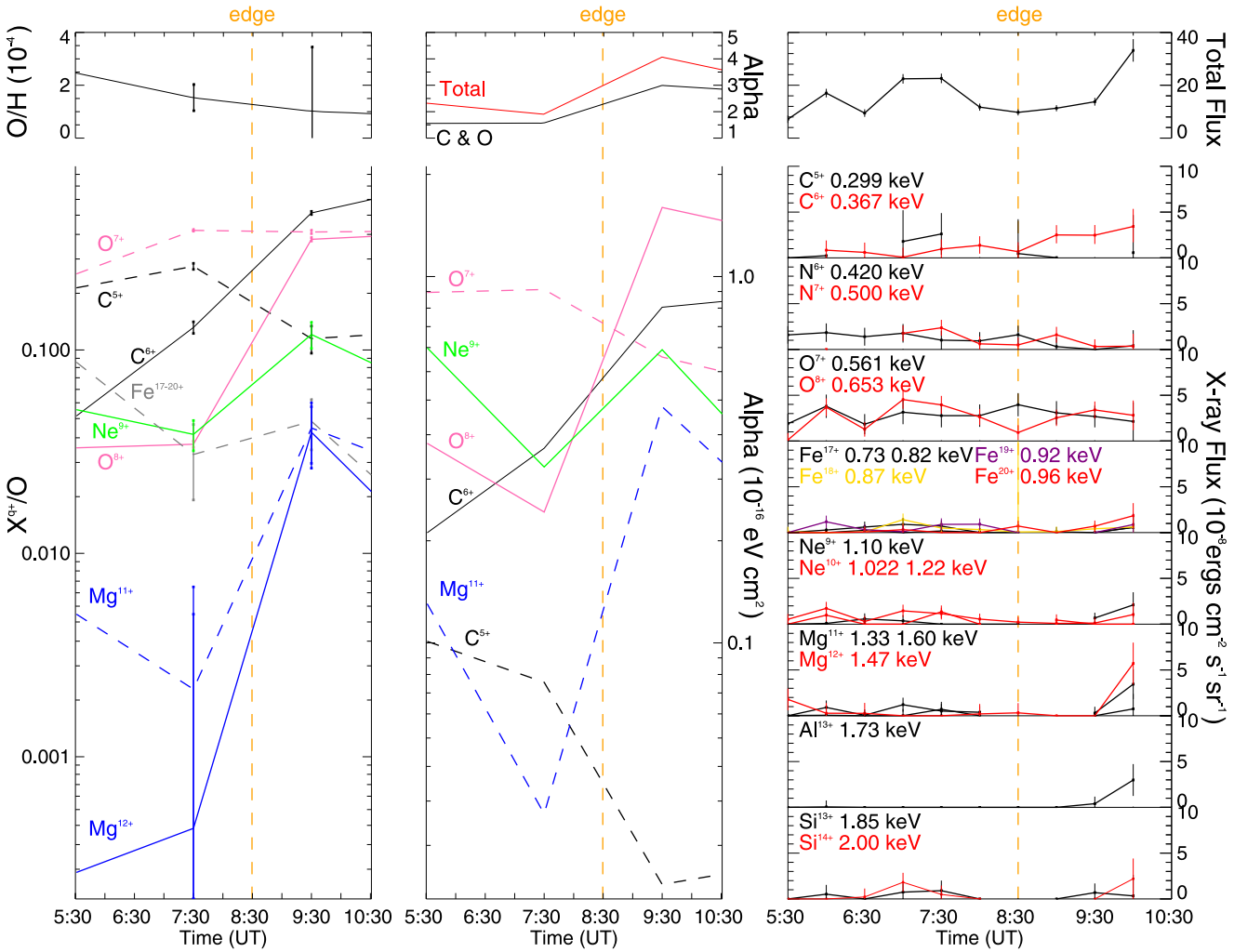

Figure 4. Left panel: ratios of each ion to oxygen ions (bottom) and ratios of oxygen ions to solar wind protons (top) as measured by ACE. Middle panel: calculated alphas for each ion (bottom) and sum of calculated alphas (top). Right panel: fitted X-ray fluxes for each ion line emission (bottom) and for the total SWCX emission (top). Vertical orange dashed line: estimated ICME leading edge.

X-ray observations. However, this would complicate the assessment of SWCX backgrounds in astronomical observations because, in addition to the solar wind proton flux, the composition and ionic state of ions must also be examined.

4.2. Spectral Diagnosis of SWCX Emissions

To date, in situ measurements have been the only technique used to acquire the composition and valence of solar wind ions. Although the Solar Wind Ion Composition Spectrometer (SWICS) instrument on ACE can detect a wide range of energies, certain ion species are excluded and certain ions in higher charge states are lacking, due to instrument and data analysis limitations (Gloeckler et al. 1998). However, the fitted X-ray flux for C^{5+}, C^{6+}, Ne^{9+}, Mg^{11+}, and Mg^{12+} was consistent with the solar wind ion abundance ratios observed in situ by ACE, confirming that the spectral diagnosis of SWCX emissions could be a new method for remotely analyzing the distributions of high-state ions in solar wind. Once the SMILE mission targeting Earth's magnetosphere is launched, we will understand more clearly the changes in SWCX spectra due to incoming solar wind ions. Note this method is limited by a lack of accurate cross sections and we look forward to further collaboration with atomic physicists to improve the model (Liang et al. 2014, 2021).

4.3. SWCX Efficiency Factor (Alpha)

The constant alpha, involving all species and charge states, is generally used in empirical SWCX models. Conventional values include 1.6×10^{-16} (Schwadron & Cravens 2000), 9.4×10^{-16} (slow wind), and 3.3×10^{-16} eV cm^2 (fast wind) (Pepino et al. 2004). It is evident that using a fixed alpha that may have values spanning over an order of magnitude does not reflect the real interactions of the solar wind and magnetosphere. In this study, we calculated the time-varying alpha using ion abundance ratios measured by ACE. The average alpha derived for C^{5+}, C^{6+}, O^{7+}, O^{8+}, Ne^{9+}, and Mg^{11+} was 2.1×10^{-16} (ICME-driven sheath) and 3.6×10^{-16} eV cm^2 (ICME). It is clear that alpha in the ICME was 1.7 times that of the ICME-driven sheath. However, considering the decrease in solar wind proton flux, the intensity of SWCX emissions in the ICME remained uncertain. In any case, the enhancement of alpha in the ICME does provide favorable conditions for soft X-ray observations of SWCX emissions. This result is advantageous for the SMILE mission because the observing schedule happens to align with the solar maximum, during which the ICME frequency is higher

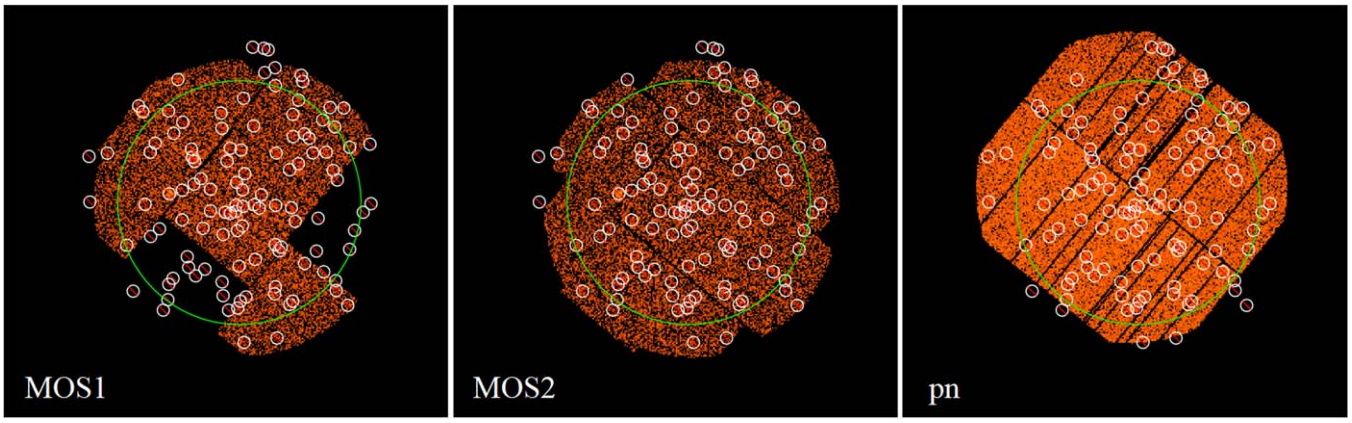

Figure 5. Images from individual EPICs in the energy range of 0.3–2.0 keV. The small white circles with red slashes represent point sources to be removed. The large green circle indicates the extracted region used for analysis.

(Zhao et al. 2016). Furthermore, we suggest using a time-correlated or two-stage alpha to better estimate SWCX soft X-ray emission intensity in an ICME.

5. Conclusion

This study represents the first attempt to distinguish magnetospheric SWCX emissions during the impact of an ICME and its driven sheath on Earth. We find that although the solar wind proton flux in the ICME is low, the abundance of high-valence ions is high, so SWCX emission intensity in the ICME remains strong. In addition, this study represents the rare joint observation of ACE and XMM-Newton in an ICME event and leads to two conclusions. First, the spectral diagnosis of SWCX emissions can provide a new approach for remotely analyzing high-state ion distributions in solar wind. Second, a time-correlated or two-stage alpha is proposed to better estimate SWCX soft X-ray intensity during ICME impact. Finally, it is suggested to consider both solar wind proton flux and ion abundance when evaluating the SWCX background during astronomical observations.

This work was supported by NNSFC grants 41731070, 42074202, 41774173, and 41974211; the Key Research Program of Frontier Sciences CAS (grant No. QYZDJ-SSW-JSC028); the Strategic Pioneer Program on Space Science; CAS grant Nos. XDA15052500, XDA15350201, and XDA15017000; and in part by the Research Fund from the Chinese Academy of Sciences and the Specialized Research Fund for State Key Laboratories of China. T.S. is also supported by the Young Elite Scientists Sponsorship Program (CAST—Y202045). T.S. thanks ISSI in Bern Switzerland for support of the International Team N523 "Imaging the Invisible: Unveiling the Global Structure of Earth's Dynamic Magnetosphere." D.K.'s heliospheric SWCX modeling work was supported by CNES and was conducted using the High Performance Computer and Visualisation Platform (HPCaVe), hosted by UPMC—Sorbonne Université. We thank LetPub (www.letpub.com) for linguistic assistance and pre-submission expert review.

Appendix
Region for Analysis

The European Photon Imaging Camera (EPIC) contains three X-ray CCD cameras: MOS1, MOS2, and pn. All three cameras operating in full-frame mode were used for SWCX emission analysis. First, we reprocessed ODFs to obtain calibrated and concatenated event lists by running EPIC reduction meta-tasks (emproc for MOS and epproc for pn). We then selected X-ray events by applying the following filter expressions: $(PATTERN <= 12)\&\&(\#XMMEA\_EM)$ for MOS and $(PATTERN == 0)\&\&(FLAG == 0)$ for pn. This not only removed events from regions of known bright pixels or near CCD boundaries, it also optimized the energy resolution of pn in the energy range of interest (<2 keV). Third, as shown in Figure 5, we directly excluded the CCD6 for MOS1 because it operated in anomalous states where the background below 1 keV was strongly enhanced (Kuntz & Snowden 2008). Finally, we selected those events within a circular region of radius 11.7' centered on the common sky position (01:12:04.3067, +49:28:55.649, J2000).

ORCID iDs

Yingjie Zhang https://orcid.org/0000-0003-4777-9552
Tianran Sun https://orcid.org/0000-0002-3042-247X
Chi Wang https://orcid.org/0000-0001-6991-9398
Li Ji https://orcid.org/0000-0001-7500-0660
Jennifer. A. Carter https://orcid.org/0000-0002-0981-2895
Steve Sembay https://orcid.org/0000-0002-3700-9784
Dimitra Koutroumpa https://orcid.org/0000-0002-5716-3412
Ying D. Liu https://orcid.org/0000-0002-3483-5909
Guiyun Liang https://orcid.org/0000-0003-1628-5058
Wenhao Liu https://orcid.org/0000-0002-0924-9668
Wei Sun https://orcid.org/0000-0002-5456-0447
Xiaowei Zhao https://orcid.org/0000-0002-4016-5710

References

Asakura, K., Matsumoto, H., Okazaki, K., et al. 2021, PASJ, 73, 504
Bodewits, D., Christian, D. J., Torney, M., et al. 2007, A&A, 469, 1183
Branduardi-Raymont, G., Bhardwaj, A., Elsner, R. F., et al. 2007, P&SS, 55, 1126
Branduardi-Raymont, G., Sembay, S. F., Eastwood, J. P., et al. 2012, ExA, 33, 403
Branduardi-Raymont, G., Wang, C., Escoubet, C., et al. 2018, SMILE Definition Study Report, European Space Agency, ESA/SCI, No. 1, doi:10.5270/esa.smile.definition_study_report-2018-12
Carter, J. A., & Sembay, S. 2008, A&A, 489, 837
Carter, J. A., Sembay, S., & Read, A. M. 2010, MNRAS, 402, 867
Carter, J. A., Sembay, S., & Read, A. M. 2011, A&A, 527, 837

Carter, J. A., Sembay, S., & Read, A. M. 2012, AN, 333, 313
Collier, M. R., Porter, F. S., Sibeck, D. G., et al. 2012, AN, 333, 378
Collier, M. R., Snowden, S. L., Sarantos, M., et al. 2014, JGRE, 119, 1459
Cravens, T. 2000, ApJL, 532, L153
Cravens, T. E. 1997, GeoRL, 24, 105
Dennerl, K., Lisse, C. M., Bhardwaj, A., et al. 2006, A&A, 451, 709
Ezoe, Y., Ebisawa, K., Yamasaki, N. Y., et al. 2010, PASJ, 62, 981
Ezoe, Y., Miyoshi, Y., Yoshitake, H., et al. 2011, PASJ, 63, S691
Gloeckler, G., Cain, J., Ipavich, F., et al. 1998, SSRv, 86, 497
Henley, D. B., & Shelton, R. L. 2010, ApJS, 187, 388
Henley, D. B., & Shelton, R. L. 2012, ApJS, 202, 14
Ishi, D., Ishikawa, K., Numazawa, M., et al. 2019, PASJ, 71, 23
Ishikawa, K., Ezoe, Y., Miyoshi, Y., et al. 2013, PASJ, 65, 981
Kaaret, P., Koutroumpa, D., Kuntz, K. D., et al. 2020, NatAs, 4, 1072
Khan, H., & Cowley, S. 1999, AnGeo, 17, 1306
Koutroumpa, D. 2012, AN, 333, 341
Koutroumpa, D., Acero, F., Lallement, R., Ballet, J., & Kharchenko, V. 2007, A&A, 475, 901
Koutroumpa, D., Collier, M. R., Kuntz, K. D., Lallement, R., & Snowden, S. L. 2009, ApJ, 697, 1214
Koutroumpa, D., Lallement, R., Kharchenko, V., et al. 2006, A&A, 460, 289
Kuntz, K. D., & Snowden, S. L. 2008, A&A, 478, 575
Liang, G., Zhu, X., Wei, H., et al. 2021, MNRAS, 508, 2194
Liang, G. Y., Li, F., Wang, F. L., et al. 2014, ApJ, 783, 124
Lisse, C. M., Dennerl, K., Englhauser, J., et al. 1996, Sci, 274, 205
Liu, Y. D., Chen, C., & Zhao, X. W. 2020, ApJL, 897, L11
Liu, Y. D., Luhmann, J. G., Kajdic, P., et al. 2014, NatCo, 5, 3481
Liu, Y. D., Zhao, X. W., & Hu, H. D. V. A. Z. B. 2019, ApJS, 241, 15
Pepino, R., Kharchenko, V., Dalgarno, A., & Lallement, R. 2004, ApJ, 617, 1347
Richardson, I., & Cane, H. 2004, JGRA, 109, A09104
Richardson, I. G. 2014, SoPh, 289, 3843
Richardson, I. G., & Cane, H. V. 2010, SoPh, 264, 189
Schwadron, N., & Cravens, T. 2000, ApJ, 544, 558
Shue, J., Chao, J., Fu, H., et al. 1997, JGRA, 102, 9497
Sibeck, D. G., Allen, R., Aryan, H., et al. 2018, SSRv, 214, 79
Snowden, S. L., Collier, M. R., Cravens, T., et al. 2009, ApJ, 691, 372
Snowden, S. L., Collier, M. R., & Kuntz, K. D. 2004, ApJ, 610, 1182
Sun, T. R., Wang, C., Sembay, S., et al. 2019, JGRA, 124, 2435
Sun, T. R., Wang, C., Wei, F., & Sembay, S. 2015, JGRA, 120, 266
Sun, T. R., Wang, X., & Wang, C. 2021, JGRA, 126, A028314
Wang, C., & Branduardi-Raymont, G. 2020, ChJSS, 40, 700
Zhao, L., Landi, E., Fisk, L. A., & Lepri, S. T. 2016, in AIP Conf. Proc. 1720, Solar Wind 14, ed. L. Wang et al. (Melville, NY: AIP), 020007
Zurbuchen, T. H., & Richardson, I. G. 2006, SSRv, 123, 31